https://doi.org/10.5194/egusphere-2025-2291
Preprint. Discussion started: 28 May 2025

Near-continuous observation of soil surface changes at single slopes with high spatial resolution via an automated SfM photogrammetric mapping approach

Oliver Grothum[1], Lea Epple[1], Anne Bienert[1], Xabier Blanch[2], Anette Eltner[1]

[1]Institute of Photogrammetry and Remote Sensing, TUD Dresden University of Technology, Helmholtzstr. 10, 01069 Dresden, Germany
[2]Department of Civil and Environmental Engineering, Universitat Politècnica de Catalunya, 08034 Barcelona, Spain

Correspondence to: Oliver Grothum (oliver.grothum1@tu-dresden.de), Anette Eltner (anette.eltner@tu-dresden.de)

Abstract. Soil erosion represents a major global threat, necessitating a detailed understanding of its spatial and temporal dynamics. Advanced geospatial technologies such as time-lapse structure-from-motion (SfM) photogrammetry provide high-resolution monitoring of surface changes. This study presents a novel event-driven approach for near-continuous monitoring of hillslope surface dynamics over a multi-annual period. The system employed synchronized DSLR (digital single-lens reflex) cameras at three slope stations, triggered by a rain gauge and a daily timer. Ground control points (GCPs) were surveyed with millimeter accuracy to ensure precise georeferencing.

An automated Python-based workflow was developed to synchronize images, detect GCPs using a convolutional neural network (CNN), generate daily digital 3D surface models via SfM, and compute 3D surface models of difference (DoDs). The absolute accuracy of SfM point clouds ranged between 8 mm and 12 mm on average, primarily due to registration errors, with lower deviations (< 5 mm) in central areas after height adjustment. Relative accuracy decreased concentrically with distance from the cameras, with level of detection (LoD) values between 5 mm and 25 mm depending on distance and location.

Time series analysis revealed surface changes driven by rainfall, snowmelt, and agricultural activity. The most significant changes often occurred shortly after tillage, even with minimal rainfall, indicating both erosional and non-erosional processes. A strong negative correlation between rainfall and elevation loss was especially evident within the first seven days following tillage. Seasonal surface lowering of 3-5 cm during winter and occasional positive changes due to frost or vegetation growth were also observed. The monitoring system and workflow are transferable, and the resulting high-resolution datasets are valuable for analyzing erosion dynamics and validating soil erosion models.

1 Introduction

Soil erosion represents a significant global threat to both soil security and human security, contributing to land degradation and compromising vital ecosystem functions (Doetterl et al., 2016, Borrelli et al., 2017). Effective land management and soil conservation require a detailed understanding and quantification of erosion processes across spatial and temporal scales (e.g., Jetten & Favis-Mortlock, 2006, Fiener et al., 2020). A variety of soil erosion models have been developed to assess erosion potential and support mitigation strategies, ranging from empirical approaches such as the Universal Soil Loss Equation (USLE) and its revised form (RUSLE), to process-based models like the Water Erosion Prediction Project (WEPP) (e.g., Karydas et al., 2014, Panagos et al., 2015, Batista et al., 2019, Epple et al., 2020). While the application of these models is well established there remains a need for harmonizing methodologies and improving model evaluation strategies (e.g., Kohrell et al., 2023, Eltner et al., 2025), which critically depend on the quality and resolution of the input data (Doetterl et al., 2016, Batista et al., 2019, Fiener et al., 2020).

The accuracy of such models is closely tied to how well the surface and topographic conditions are characterized. Traditional methods, such as rainfall simulation experiments and sediment yield measurements, have been augmented in recent years by

https://doi.org/10.5194/egusphere-2025-2291
Preprint. Discussion started: 28 May 2025

advanced geospatial technologies (e.g., Hänsel et al., 2016, Balaguer-Puig et al., 2017, Li et al., 2023). High-resolution surface data obtained through structure-from-motion (SfM) photogrammetry and terrestrial laser scanning (TLS) offer promising avenues for capturing surface dynamics associated with processes such as interrill and rill erosion (e.g., Eltner et al., 2015, Cândido et al., 2020, He et al., 2022, Dai et al., 2022, Evans et al., 2024). These methods enable the detection of subtle changes in surface microtopography and provide spatially continuous information essential for model calibration and validation (Epple et al., 2022).

The generation and processing of three dimensional (3D) point clouds for observing and understanding earth surface processes has become a cornerstone of geomorphological research. Early systems fsr change detection relied on simple camera setups combined with external depth data (e.g., Krimmel & Rasmussen, 1986; Schwalbe et al., 2016). With the advent of SfM photogrammetry, studies began constructing time series of 3D surface data directly from image sequences, often collected through manually triggered, synchronized DSLR (digital single-lens reflex) setups (Eltner et al., 2017) or automated low-cost systems using microcontrollers and wireless data transmission (Kromer et al., 2019; Blanch et al., 2023, 2024). Additionally, laser scanners mounted on permanent structures have enabled continuous monitoring of highly dynamic environments such as beaches (Vos et al., 2022), supporting the development of advanced four dimensional (4D) change detection algorithms (Anders et al., 2021).

In the context of soil erosion research, this technological progress enhances our ability to observe and analyze processes like splash, interrill, and rill erosion with unprecedented detail. Artificial rainfall simulations remain a key approach for producing controlled erosion data on standardized plots (Michael, 2014; Hänsel et al., 2016), which serve as benchmarks for calibrating and validating erosion models (Schindewolf & Schmidt, 2012). However, extending these observations to the field scale is critical for upscaling model applications (Eltner et al., 2018), as it captures the spatial heterogeneity and complexity of real-world erosion dynamics.

In this study, we present a novel, event-triggered camera system developed for continuous monitoring of soil surface changes on a experimental field on a hillslope over a period of 3.5 years. The system uses synchronized cameras and a partly open-source workflow to automatically organize image data, detect ground control points (GCP), and reconstruct daily 3D surface models (i.e., 3D point clouds). These models are assessed using reference data from TLS and uncrewed aerial vehicle (UAV) photogrammetry to measure absolute accuracy, while the relative accuracy and the level of detection (LoD) are estimated from multiple 3D surface models acquired under unchanged surface conditions. This approach enables high spatial and temporal resolution observations of soil surface changes caused by natural rainfall, snowmelt, and agricultural practices, capturing a range of erosive processes and supporting multi-scale model development and validation.

2 Experimental design

To quantify and monitor soil surface change dynamics during natural rainfall events, we propose a semi-autonomous observational system that integrates event-triggered camera control with time-lapse photogrammetry.

2.1 System setup

A monitoring system is introduced that was setup on a freshly turned grassland on an agricultural test site in the hilly loess landscape of Saxony, Germany, to capture soil surface changes nearly continuously over a prolonged period at the field scale. The field was kept free of vegetation by frequently grubbering the soil at depths of 5-20 cm. The experimental site has a north-northeast orientation, and the slope reaches a steepness of up to 14%. The soil is a sandy silt with a soil organic carbon content of 1.25% (as of July 2021), making it prone to erosion.

The hillslope was observed over a length of about 60 m and a width of about 15 m. Three monitoring systems were installed: one at the top, one in the middle, and one at the bottom of the slope. Each observation system consisted of two A-shaped

https://doi.org/10.5194/egusphere-2025-2291
Preprint. Discussion started: 28 May 2025

constructions, carrying a wooden horizontal beam (Fig. 1). On these cross struts, five DSLR cameras were mounted, which e
80 triggered by microcontrollers. The original system contained one metal traverse and two angular elements to maintain horizontal stability. However, during a storm, two of the monitoring systems collapsed, prompting a redesign of the weaker construction elements. The traverses were subsequently supported by additional horizontal planks and two stronger angular wooden elements installed below the traverses.

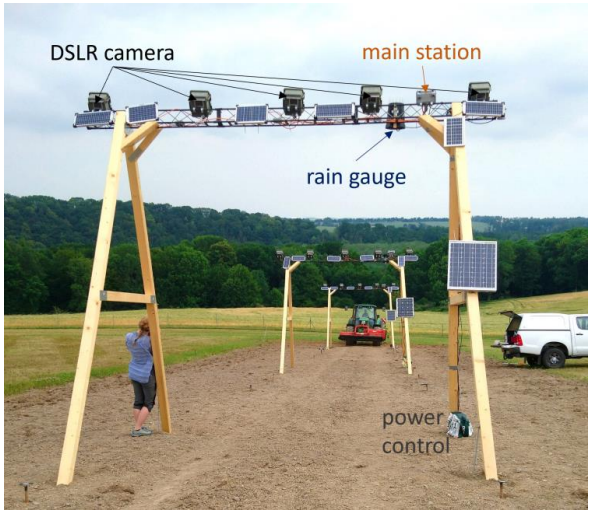

85 **Figure 1: Construction of the soil surface monitoring system at the lower, middle, and upper slope observing the field at a hillslope with synchronized DSLR (digital single-lens reflex) cameras that were triggered by a rain gauge. The image shows the regular down/upslope tillage of the field.**

2.2 Data acquisition

Each camera on the rigs was placed in a waterproof housing. Power was supplied by an external 7 Ah sealed lead-acid battery,
90 which was charged by an external 10 W solar panel placed near the camera housing. The triggering of the cameras occurs during two instances – controlled by two microcontrollers: a) a scheduled trigger and b) an event-based trigger due to rainfall. In the former instance (a), a permanently running Arduino Micro Pro, connected to a real-time clock (RTC), sends a trigger signal every day at 10:00 a.m. CET (Fig. 2). The microcontroller was powered by the same battery-solar panel system as the cameras.

95 The second, event-based trigger (b) signal originated from the main station, which was controlled by an Arduino MKR FOX 1200 (Fig. 3) and which was connected to an RTC module. The main station controls the synchronized camera trigger. The microcontroller of the main station was coupled to a rain gauge. The gauge consisted of a reed switch, which was activated every time 0.2 mm of rain had been collected by the tipping bucket. This caused a circuit to close, which was registered by the Arduino. Every time a trigger signal was received, the main station microcontroller switched the state of a relay that was
100 connected in parallel to all five cameras, allowing for synchronized image capture. In addition to the rain-controlled trigger, a synchronized daily image trigger was also realized by the main station at 10:00 a.m. CET by the main station (in addition to the daily trigger by the local microcontroller of b) (in addition to the local daily trigger of b). Besides the trigger connections, the main controller was connected to additional weather sensors, i.e., a DTH11 sensor to collect air temperature and humidity, and a soil moisture sensor. The sensor readings were transmitted via IoT (Internet of Things) using the IoT infrastructure
105 provided by the company Sigfox that offers a low power wide area network. To save power, the microcontroller was set into a deep sleep mode and woke only upon the daily alarm interruption signal (at 10:00 a.m. CET) or the external interrupt signal triggered by the tipping of the rain gauge bucket. A typical lead-acid car battery (50 Ah), charged by a 70 W solar module, was used to power the main station.

https://doi.org/10.5194/egusphere-2025-2291
Preprint. Discussion started: 28 May 2025

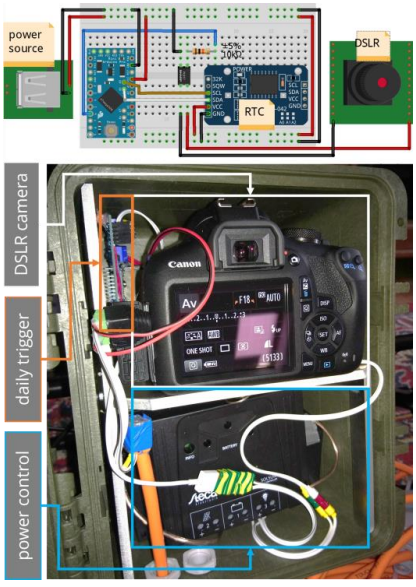

Figure 2: Housing with its content of one of five cameras installed at each monitoring rig. The top sketch (using fritzing.org) illustrates the wiring of the daily trigger system using an Arduino (DSLR = digital single-lens reflex, RTC = real time clock).

The DSLR cameras were the Canon EOS D2000 models, each equipped with a zoom lens fixed at 18 mm using tape. The cameras had a 3.5 mm 3-pin jack interface for external triggering. The cameras were set to aperture priority mode to ensure geometric consistency of the internal camera orientation throughout the observation period. Exposure time was left variable to allow flexibility under different lighting conditions.

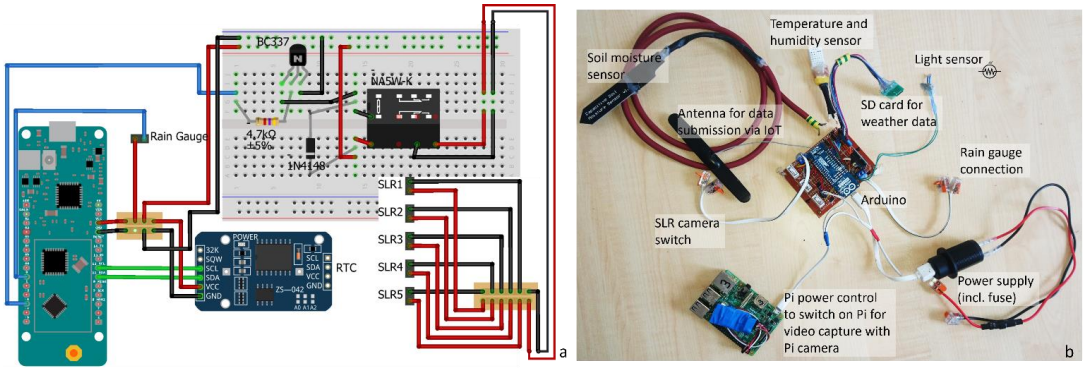

Figure 3 a) Schematics of simplified (without environmental sensors and Raspberry Pi) parallel camera triggering system (main station; using fritzing.org), using a rain gauge for rainfall measurement and camera triggering and a RTC (real time clock) for synchronous triggering at 10:00 a.m. CET b) setup used in the field including all sensors and systems (SLR = single-lens reflex).

2.3 Georeferencing

GCPs were installed in the field to orient the image measurements within a reference frame and to scale the photogrammetrically derived 3D models (Fig. 4). The GCPs consisted of white circles on a black background. The markers were attached to poles that were rammed up to one meter deep into the soil to ensure stability during the monitoring period, an important requirement for soil surface change detection (Eltner et al., 2015). The GCPs were slightly tilted towards the camera rigs to maintain good visibility and to minimize distortions from the bird's-eye view in the case of UAV data. The coordinates of the

https://doi.org/10.5194/egusphere-2025-2291
Preprint. Discussion started: 28 May 2025

GCPs were measured using a Leica TCRM 1102 total station, achieving millimeter-level accuracy. The marker position estimates were transformed from a polar into a Cartesian coordinate system based on the total station's orientation, resulting in a final coordinate for each point with an accuracy of 2 mm.

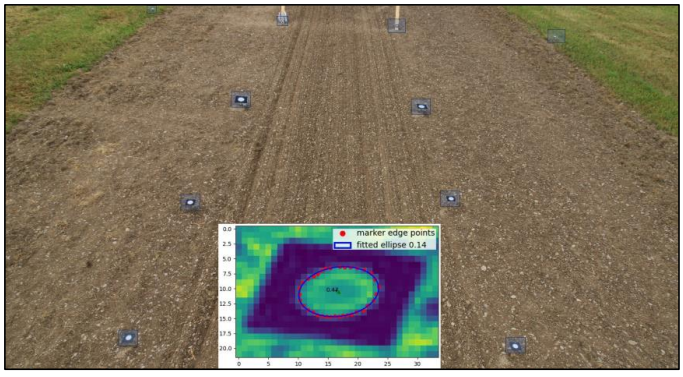

Figure 4: GCP configuration at one camera rig. The ten markers outline a trapezoidal area of interest. The small figure illustrates the ellipse fitting result for one GCP.

2.4 Reference data for the accuracy assessment

2.4.1 UAV photogrammetry

A DJI Phantom 4 RTK drone was used to capture the UAV-based imagery on 2020-08-11. Due to the low flying height of 10-15 m, required to achieve millimeter-level image resolutions, the flights and image triggering had to be performed manually. The flight pattern aimed to cover the entire area of interest with nadir images (i.e., camera gimbal angle of 90 degrees) and convergent images taken from the sides of the field at 60-degree angles. The images were processed in *Agisoft Metashape* (v1.8.3), using the standard SfM photogrammetry pipeline (e.g., Eltner & Sofia, 2020), which involved establishing the relative orientation of all images, referencing them to the local coordinate system (defined by the GCPs), and constructing a dense point cloud of the field surface.

2.4.2 Terrestrial laser scanning

To check the processed camera data for systematic errors, the soil surface was scanned with a RIEGL VZ400i terrestrial laser scanning system. The investigated slope was scanned on 2020-08-11. According to the manufacturer's specifications, the device can capture half a million points per second with an accuracy of 5 mm at a range of up to 800 m. Scanning was performed from eight different positions surrounding the hillslope. Each scan was relatively oriented to its neighboring scan using the iterative closest point (ICP) algorithm (Besl & McKay, 1992; Chen & Medioni, 1991), minimizing the mean distances between point clouds.

To transform the laser scanner point clouds into the local coordinate system, retro-reflective cylindrical targets were used to identify reference points during scanning. The cylinders were placed on the GCPs (used for the image measurements) that bounded the field. By matching the targets detected in the scanner coordinate system to the GCP points in the local system, the parameters of a rigid transformation were calculated. Applying the estimated translation and rotation parameters enabled the transformation of the scanner point cloud into the local coordinate system.

3 Methods

The automatic workflow for time lapse-based soil surface change detection is divided into five modules: a) camera calibration, b) image sorting and time attribution, c) time lapse SfM photogrammetry, d) point cloud processing for filtering the

https://doi.org/10.5194/egusphere-2025-2291
Preprint. Discussion started: 28 May 2025

reconstructed 3D surface models, and e) calculation of the DoD. The implementation is realized in Python. The workflow primarily utilizes the *numpy*, *pandas*, *matplotlib* and *OpenCV* libraries for data management, visualization and image processing. For image alignment and 3D reconstruction of the soil surfaces, the *Agisoft Metashape Python API* (v1.8.3) was used. Point cloud processing steps were performed using the Python package *CloudComPy*, which provides access to various *CloudCompare* (v2.13.2, 2024) functionalities.

3.1 Camera calibration

Calibrating cameras is a fundamental task for accurately modeling the projection ray from the object point to the image sensor plane. In this work the camera parameters of the Brown (1971) model were used, consisting of the focal length (f) and the principal point coordinates (xP, yP), representing the perpendicular intersection of the focal point with the sensor plane. In addition, image distortion is considered through radial distortion (K1, K2, K3, and K4) and decentering distortion parameters (B1, B2).

Each camera was pre-calibrated, since only a few images (i.e., five) were available for the 3D reconstruction and for each camera a different set of parameter values applied for the interior orientation. This contrasts with typical SfM applications, where many images are taken with a single camera. The aim was to avoid overparameterization by estimating distortion parameters beforehand and deriving reliable approximations of focal length and principal point, which were then only fine-tuned during the reconstruction of the area of interest (Eltner et la., 2017).

To estimate the interior geometry parameters, images of a calibration field with markers of known geometry were captured and processed in a least-squares bundle adjustment to derive both the interior and exterior orientations (Luhmann et al., 2016). During the pre-calibration approximately 50 coded markers were arranged in a square pattern to serve as a temporary target field (e.g., Eltner & Schneider, 2015). To decorrelate the focal length and camera-to-object distance estimations, additional markers were placed on small boxes to introduce height variations in the calibration field (Fig. 5). Marker coordinates were measured with a measuring tape (within millimeter-accuracy) to define a local reference frame. These coordinates were refined during the bundle adjustment and were not treated as fixed control points as they were not measured with superior accuracy and thus considered as approximate values. Images were taken by each camera while moving around the calibration field, following the acquisition scheme proposed by Godding & Luhmann (1992) to minimize parameter correlations. Calibration was performed using *Aicon* (version 1.12). As *Aicon*'s calibration outputs are not directly compatible with *Agisoft Metashape*, the calibration images, object-space coordinates, and image measurements of the coded targets were exported from Aicon and imported to *Agisoft Metashape*. The coded target coordinates are introduced as GCPs with assigned accuracies of 0.1 mm to constrain them during parameter estimation. The resulting parameters were saved and later applied in the time lapse SfM processing step.

Figure 5: Control point scheme for camera calibration next to the experimental field.

https://doi.org/10.5194/egusphere-2025-2291
Preprint. Discussion started: 28 May 2025

3.2 Time attribution

Synchronizing cameras in this setup is not straightforward, as the cameras are triggered externally and both the internal camera clocks and the RTCs of the Arduinos Micro Pro units are subject to temporal drift. Each system can drift differently over time. Mallalieu et al. (2017) reported a drift of up to 30 minutes in a wildlife camera-based monitoring system operating over several months. Besides the temporal drift, inconsistencies in the image series can occur. Cameras may occasionally fail to capture an image despite receiving a trigger signal. To address these challenges, an automatic approach to temporally align the camera data (Fig. 6) was designed. One camera is selected as the reference, and the time offsets of the remaining cameras are estimated based on the daily 10:00 a.m. CET capture. Subsequently, the time differences for each rain gauge-triggered image are retrieved.

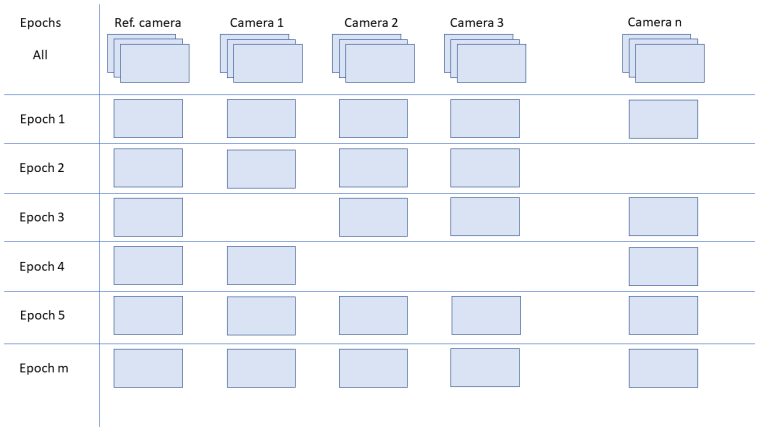

Figure 6: Temporal camera alignment considering real-time clock (RTC) drift and potential data capture failure during the long-term observation. The remaining cameras are matched to the reference.

The entire time-series was divided into monthly sets of images to retrieve temporally aligned batches. Within each batch, the camera with the highest number of captured images during a user-defined timespan was selected as the reference. The length of this timespan depends on the reliability of the daily capturing system. A minimum of two days is required to estimate the temporal offset between two cameras. When no outages occur, one month of data is typically sufficient for estimating the drift in offset. However, if outages span multiple days, it is advisable to include a longer period – e.g., three months – for accurate offset estimation. Accordingly, throughout the experiment, reference camera selection, offset calculation, and time attribution were performed in rolling three-month batches. For each image in the reference series, the corresponding image from each of the remaining cameras was identified by minimizing the time difference between the reference image and the image to be assigned, which ideally approached zero. The time offsets between the reference and the remaining cameras were determined monthly. Note, the reference camera can vary from month to month.

To synchronize the cameras, time points were collected, where no more than two images per day were taken within a short sequence. These instances represent the daily triggers at 10:00 a.m. from the main station and the Arduino Micro Pro backup system. To calculate the offset between time series, two different time series had to be considered. A linear model was fitted to both, and the one with the lower root mean square error (RMSE) was selected to define the offset model between reference camera and the other cameras. This model was stored as a lookup table for time alignment.

Applying the offset derived from the best-fitted line to the image timestamps allowed identification of corresponding images across camera systems. The time series from the main trigger station was generally selected for correction, as if exhibited a more consistent temporal offset than the Arduino Micro Pro backup systems. The RMSE value of the line fit was used as a threshold. Thereby, a 3-sigma rule was applied: the absolute time difference between the reference camera and the offset-

https://doi.org/10.5194/egusphere-2025-2291
Preprint. Discussion started: 28 May 2025

corrected camera had to be less than three times the RMSE; otherwise, the temporal matching of images failed (Fig. 7). Image sequence assignment – i.e., determining which image belongs to the first or second trigger event – was based on the capture timestamp. The image captured earlier belongs to the first series, the latter to the second one, under the assumption that both series maintain distinct offsets and do not cross (i.e., change order) within the three-months observation window. As shown in figure 7, the distinguishable trait is the variance of its single capturing times to the fitted offset line. The difference of variance is attributed to discrepancies in clock accuracy between the main trigger station and the backup system. It is assumed that the blue line with the lowest variance is triggered by the main station, therefore that series is considered for the offset calculation.

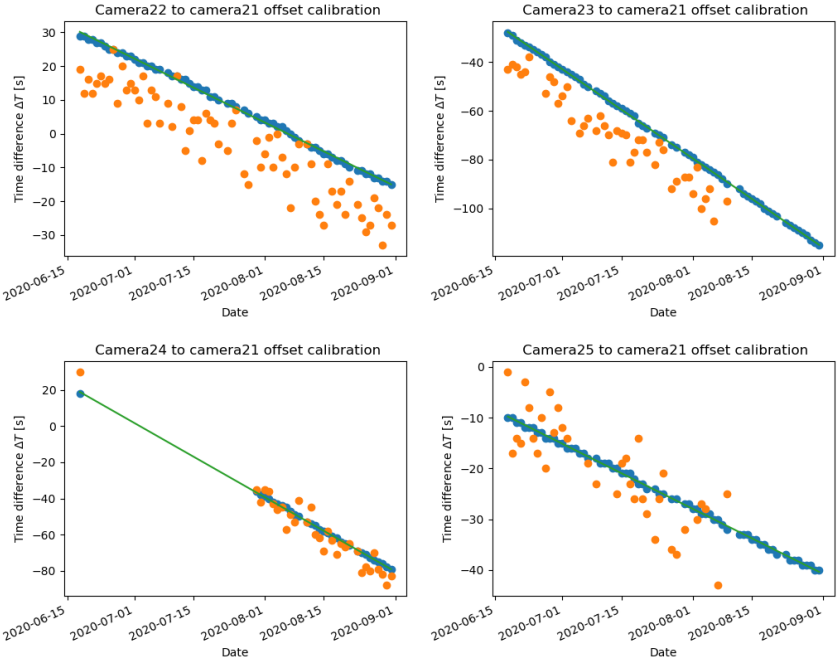

Figure 7: Time offset calibration for each secondary camera to the chosen reference camera for June, July and August 2020. Blue dots refer to capturing times of images, whose triggering has been induced by the main station. Orange points refere to the images triggered by each individual back up system. The green line defines the least squares adjusted line of the blue points.

3.3 Ground control point tracking

Tracking GCPs across all images poses a complex task, as different capture conditions affect the quality and reliability of automatic detection. Initially, a commonly used tracking algorithm was employed – template matching via normalized cross correlation – however this approach did not provide sufficient results due to changing lighting conditions throughout the seasons and weather conditions. Therefore, an end-to-end Keypoint-CNN was adapted and trained specifically with images triggered by the soil erosion cameras. This approach performs a more robust template matching, using bounding box to detect the GCP in the images and a key point detector to identify the coordinate of the center of the GCP. Each image was cropped in evenly shaped, overlapping patches of 512x512 pixels to ensure that GCPs located near patch boundaries were not missed or split. However, this overlap occasionally resulted in the same GCP being detected multiple times within a single image. To resolve redundant detections, a k-means clustering approach based on the detected coordinates was applied to group potential GCP candidates. The final coordinate for each GCP was then calculated by averaging the clustered coordinates. For further technical details, refer to Blanch et al. (2025).

https://doi.org/10.5194/egusphere-2025-2291
Preprint. Discussion started: 28 May 2025

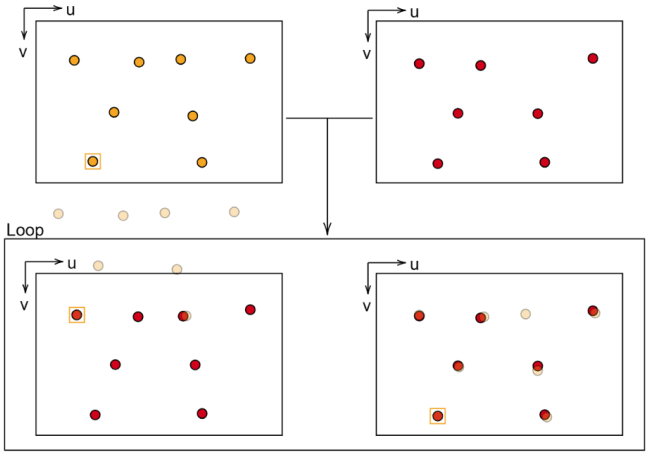

Figure 8: Principle of the GCP labeling process. The orange dots represent the reference position of the GCPs, which are labeled, the red dots are the found GCP without a label on the subsequent images. The orange bounded GCP is the query point for a single iteration of this process. The bottom images show the loop process, where the reference points are shifted onto each found GCP in the target image. The left image inside the loop shows a bad overlap and is therefore rejected, whereas the right image shows good congruency and the label of the reference query point is applied to the target GCP. u and v refer to the image coordinate system axes.

Since the GCP tracking does not assign label information, i.e., an ID to be assignable to the corresponding 3D coordinate in the local coordinate system, an approach was developed to label each marker and filter out erroneously tracked GCPs. For each month, the first image from each camera is selected as a reference image, in which the image coordinates of the GCPs are manually measured and labeled (Fig. 8). These labeled reference measurements are then used to assign labels to GCPs in subsequent images. A nearest-neighbor search for this case is a simple version but prone to errors, for instance due to non-tracked GCPs. To improve robustness, the algorithm incorporates the relative spatial position of surrounding GCPs. The algorithm iterates over each GCP in the manually labeled reference frame. The coordinates of all GCPs are reduced by the image coordinate of the query GCP. The reduced coordinates are then projected into the image frame of the subsequent images. The center of the projected net is moved onto each local detected GCP. If the projected net is congruent to the GCP image positions of the target image, the projected GCP and the measured GCP should align with some minor error. The constellation with the most overlapping measurements within a certain threshold (50 pixel in this study) is accepted. If fewer than four matching points are found, the label is not assigned, as the GCP is deemed unreliable in that image. This procedure is repeated for every GCP in the reference image, which is then treated as the query point.

To further improve accuracy, eventually an ellipse fitting step is applied to refine the GCP position to the center of the detected ellipse, enabling sub-pixel precision. Further manual correction was applied where tracking and ellipse fitting failed. To independently verify the accuracy of the SfM-based 3D reconstruction, at least one GCP was defined as check point (CP) and hence excluded from the bundle adjustment.

3.4 Soil Reconstruction

3.4.1 SfM photogrammetry

In this study, SfM photogrammetry was used for digital soil surface reconstruction. The process involves as a first step the detection of key points, which are distinct features found in multiple overlapping images. These key points are matched by comparing multi-dimensional vectors that encapsulate the local image neighborhood. Those matched features, also called tie points, serve as the primary observation for image alignment. The image observations are used within a bundle adjustment to

https://doi.org/10.5194/egusphere-2025-2291
Preprint. Discussion started: 28 May 2025

estimate the parameters of the image network geometry. This adjustment simultaneously refines the internal camera parameters, camera poses (positions and orientations), and the 3D coordinates of the tie points through triangulation across multiple views. Finally, georeferencing can be done considering the GCP's image and object coordinates as additional constraints in the bundle block adjustment. With the established image network geometry, a dense point cloud can be calculated. This point cloud offers a highly accurate 3D representation of the soil surface, with a 3D coordinate estimated for nearly every pixel.

3.4.2 Time lapse data processing

The time lapse processing workflow is schematically illustrated in Fig. 9. The 3D reconstruction step is initiated by associating each image with its respective interior calibration parameters and organizing them chronologically using the previously computed attribution table. The image sets are imported into *Agisoft Metashape* and organized into chunks representing distinct reconstruction units.

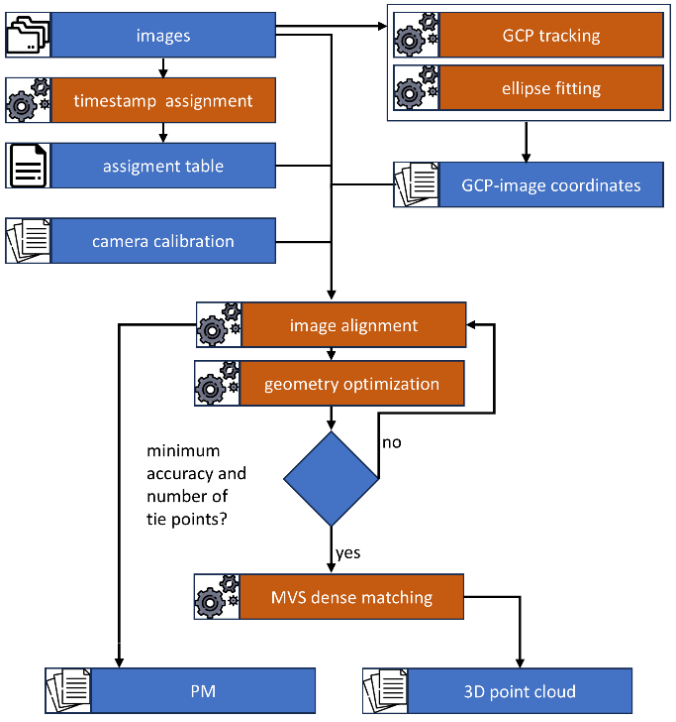

Figure 9: SfM photogrammetry workflow for time lapse data (GCP = ground control point, MVS = multi view stereo, PM = precision map).

Next, the tracked GCP locations are imported, and the image alignment is performed relative to the local coordinate system. During this alignment step, the interior camera parameters are optimized, although only the focal length and principal point are adjusted. During the alignment step, the number of tie points and the quality of the image measurements in pixel space are assessed to potentially refine the alignment. If not enough tie points are found (minimum required: 75) or the pixel error exceeds a given threshold (maximum allowed: 1.0 pixel), an iterative refinement process is applied:

1. Enable guided image matching – this allows camera calibration and initial rough alignment to improve tie point detection, and therefore increase the amount of point correspondences, albeit with longer processing times.
2. Upscaling image resolutions for image alignment – if the initial alignment (performed with downscaled images by a factor of two to increase the processing speed) is inadequate, the original image resolution is restored.
3. Increase key-point and tie-point limits.

https://doi.org/10.5194/egusphere-2025-2291
Preprint. Discussion started: 28 May 2025

4. Filtering tie points for stability and quality – for this purpose the following criteria are used: reprojection error (threshold: 1.0 pixel), reconstruction uncertainty (threshold: 25), projection accuracy (threshold: 4). Please, refer to the *Agisoft Metashape* user manual for detailed information (Agisoft LLC, 2023).

Filtered tie points are exported along with their standard deviations of the reprojections. These values are used to estimate the 3D accuracy of the sparse point cloud following the method by James et al. (2017), and serve as the basis for the precision map (PM), which spatially represents the LoD in the multi-temporal analysis. Finally, a dense point cloud is generated using *Metashape*'s high quality setting, which downscales images by a factor of two.

3.4.3 Point cloud processing

To compute the final 3D surface model for each reconstructed epoch, first the dense point clouds and their corresponding PMs must be filtered, combined, and pre-processed before they can be used for the calculation of DoDs (Fig. 10).

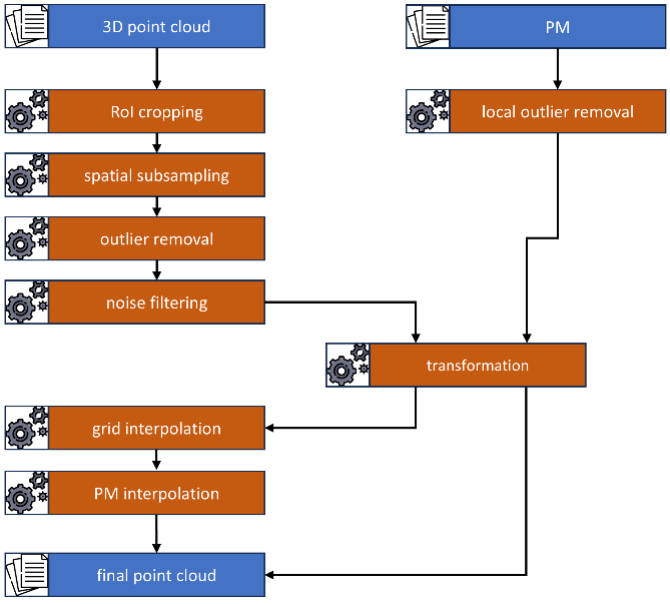

Figure 10: Point cloud processing workflow (PM = precision map, RoI = region of interest).

In the first step, all dense point clouds are cropped to the region of interest (RoI), approximately 100 m² in size. This is done by projecting the point cloud onto the XY-plane and retaining only the points that fall within a defined bounding box. Afterwards, the point cloud is spatially subsampled to reduce density, ensuring a minimum spacing of 2 mm between points. This step reduces the dataset size and filters densely populated areas more aggressively than sparser ones, while still preserving fine-scale soil surface structures.

To mitigate systematic reconstruction errors – visible as floating point clusters significantly above or below the actual reconstructed soil surface – a best-fit plane is computed through the whole point cloud, and each point's signed distance to the plane is calculated. Points exceeding three times the standard deviation (3 sigma σ) of all distances are removed. To filter remaining single outliers or little groups of outliers, a local noise filter is applied. Points are removed if the distance to the best-fit plane through its 30 nearest neighbors (NN) exceeds 2 sigma σ. Additionally, any point with less than 30 neighboring points within a 1 m radius is considered as isolated point and is therefore removed.

After the cleaning process, the point clouds are rotated parallel to the XY-plane allowing later height-based comparison parallel to the Z-axis. A plane is fitted, through the first point cloud of the series only and a transformation matrix is calculated by transforming it's normal vector to the Z-axis unity vector ez = (0,0,1) with the algorithm proposed in Möller & Hughes (1999).

https://doi.org/10.5194/egusphere-2025-2291
Preprint. Discussion started: 28 May 2025

The obtained transformation matrix is applied to the point cloud itself, its associated PM and to all following 3D point clouds and PMs. The necessity for transforming also the PMs is shown exemplary for one point in Figure . Finally, the cleaned and transformed point cloud is interpolated onto a uniform grid with a 5 mm resolution.

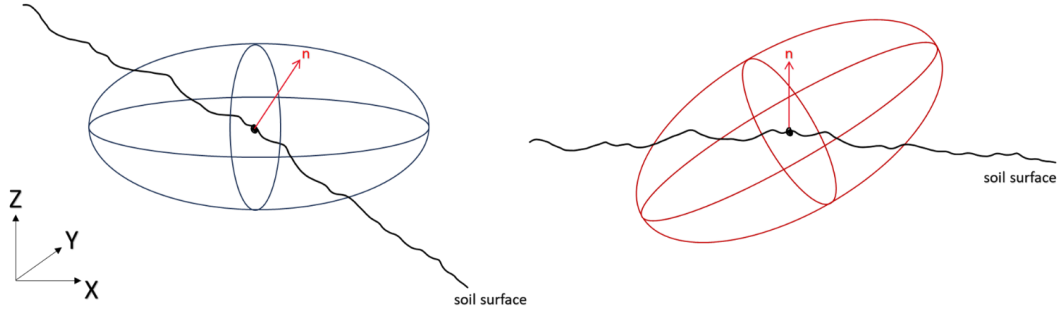

Figure 11: Applying the transformation to the point cloud itself also requires the application of the same transformation to the PM (precision maps). Considering the precision values of a certain point as a triaxial ellipsoid, the left image shows the situation in the local reference system, whereas the red vector shows the normal (n) direction and direction of the M3C2 (multiscale model to model cloud comparison). By rotation of the surface into the XY-plane, the ellipsoid must be rotated accordingly to preserve the orientation of the normal vector within it.

The dense point clouds and PMs are combined by interpolating the accuracy values from the PM onto the dense point cloud. For each point of the dense cloud, the nearest PM points within a 1 m search radius are identified. The precision values are calculated using a normal distribution kernel (eq. 1).

$$f(d) = \frac{1}{\sigma\sqrt{2\pi}} e^{-\frac{1}{2}\left(\frac{d}{\sigma}\right)^2} \quad (1)$$

Defining a sigma σ = 0.3 in this study, the weight of each PM point is determined by the distance d of the query point to the PM point.

3.4.4 Change detection

The comparison of point clouds is performed using an adapted version of the Multiscale Model to Model Cloud Comparison algorithm (M3C2; Lague et al., 2013), referred to as M3C2-PM (James et. al., 2017). In this method, a reference epoch is defined – usually the first epoch after the most recent tillage or camera system update – and all subsequent epochs are compared to this reference. In the M3C2 approach, the point normal n is calculated for a core point i using a fitted plane estimated from the neighbors NN_i to the point. A cylinder with a radius r = 50 mm is created, oriented parallel to the core point normal n_i and the origin defined by j. The cylinder intersects both point clouds, extracting subsets of points from each. Each subset is projected onto the cylinder's axis to estimate its average height value.

To consider the uncertainty of the mean distance estimation, the LoD at 95% confidence ($LoD_{95\%}$) is calculated using the propagated error values from the PMs. Since PMs are the result of error propagation of interior and exterior camera orientation during bundle adjustments, they allow for spatially correlated errors (James et al., 2017). The uncertainty is quantified by the following eq. 2.

$$LoD_{95\%}(r) = \pm 1.96\left(\sqrt{\sigma_{N1} + \sigma_{N2}} + reg\right) \quad (2)$$

Where σ_{N1} and σ_{N2} are the standard deviations of the averaged height value in normal direction for the two point clouds and reg indicates the data registration error. Eventually, significant changes for the point-wise differences will be indicated in a binary map, i.e., whether a statistically significant surface change occurred or not.

https://doi.org/10.5194/egusphere-2025-2291
Preprint. Discussion started: 28 May 2025

3.5 Accuracy assessment

The performance of the setup and data processing workflow was evaluated by comparing the reference 3D surface models obtained from TLS and UAV with the time lapse data of the same day providing absolute accuracy estimates. All point clouds were leveled to the XY-plane to maintain consistent relative orientation. Point cloud comparison was done using the M3C2 algorithm, with a projection cylinder radius set to 1.5 cm. The 3D surface model derived from the camera rig was set as the reference cloud. To simplify computation and align with the predominantly planar soil surface, the normal estimation mode was set to vertical, using the Z-direction for projection.

To obtain and check the relative accuracy of point clouds generated by the camera rig system, the PMs and their standard deviation components in X, Y and Z directions over the period from June 2020 to June 2021 were analyzed. Initially, core points from the first point cloud were selected using the farthest point sampling algorithm (Eldar et al. 1997), ensuring spatially uniform distribution. PM values from subsequent reconstructions were interpolated onto these fixed core point locations, enabling a consistent comparison of temporal PM variability across the time series. The temporal series of standard deviation values were obtained by linear interpolation from the NN in the subsequent point clouds of the series. To investigate the spatial character of the collected temporal variations, the core points were clustered into accuracy groups using *k-means clustering* by the Euclidean distance measures mean and standard deviation of its inherent time series.

3.6 Soil surface change

To evaluate the suitability of the proposed approach for monitoring soil surface changes, we analyzed data from all three monitoring posts over a measurement period of three and a half years, spanning from summer 2020 to the end of 2023. In addition to daily average change detection, a focused analysis was conducted during a period of significant rainfall on freshly tilled soil. Specifically, three 3D surface models – representing the conditions before rainfall, after light rainfall, and after heavy rainfall – were compared against a baseline 3D surface model acquired immediately after tillage and therefore a reset of the field conditions took place. The 3D surface model of 2021-08-24 was selected as the reference epoch. Comparisons were made with the 3D surface models from 2021-08-25, 2021-08-31, and 2021-09-04, representing sequential changes in surface morphology due to rainfall of varying intensity.

4 Results and discussion

The following section presents the accuracy evaluation and results of soil surface change monitoring using high-resolution 3D models derived from the multi-camera rig system. Absolute and relative accuracies are assessed, followed by detailed analysis of erosion and compaction processes in response to rainfall events. Elevation changes are interpreted across spatial and temporal scales, revealing clear links between surface dynamics, soil management practices, and weather conditions. System performance and data quality over the multi-year observation period are also discussed, highlighting both methodological challenges and potential improvements. Animations of the daily changes of the soil surface at all three slope positions throughout the years can be seen in the supplement.

4.1 Absolute accuracy

The comparison of the SfM point clouds of all three monitoring stations with the TLS and UAV reference point clouds revealed an average height deviation ranging between 8 mm and 12 mm. These discrepancies are largely attributed to registration errors of the individual systems into the local coordinate system. Registration errors of the TLS point cloud might also apply here, since it could not be checked if the pointcloud was registered accordingly. After adjusting the height offset correspondingly by applying the estimated bias, the M3C2 distances were recalculated to emphasize the local differences (Fig. 12). The central

https://doi.org/10.5194/egusphere-2025-2291
Preprint. Discussion started: 28 May 2025

regions of the RoI show the smallest distances (< 5 mm) for both, UAV and TLS comparisons, consistent of the internal precision of the UAV and TLS measurement. The deviations increase toward the edges of the RoI (5 mm – 15 mm).

Systematic spatial patterns in the deviation maps suggest the presence of spatially correlated errors in the camera rig data. This is the case for the positive height shift in the western part of the RoI observed in the middle rig's dataset, which appears in both the UAV and TLS comparisons, indicating it is not an artifact of a single reference dataset. Additional deviations arise from the different perspectives at the soil surface of the different measurement devices. For instance, wheel tracks are particularly visible in the difference image of the TLS-based comparison (differences > 20 mm). This can be explained by the oblique viewing angle of the TLS system, which increases shadowing and potential geometry-related errors (e.g., Eltner & Baumgart, 2015). The larger deviations in wheel tracks are also given in the UAV data, just with a smaller magnitude (differences approximately 10 mm), likely due to the coarser resolution resulting from the greater imaging distance compared to the camera rig.

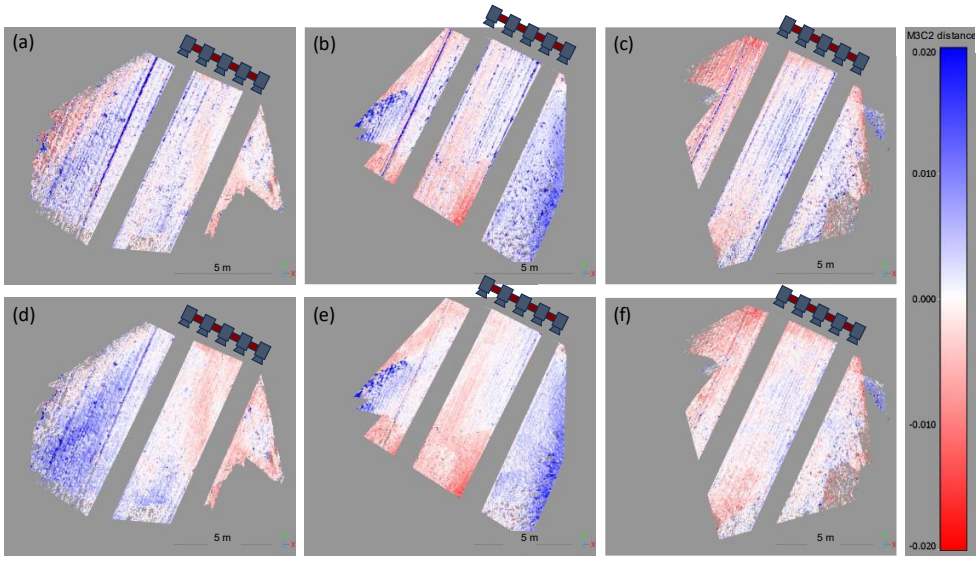

Figure 12: M3C2 (multiscale model to model cloud comparison) distances between dense clouds of observation station (left - top, middle - middle, right - bottom station) and TLS point cloud (top row) and UAV point cloud (bottom - row) respectively. Camera positions are indicated by the camera sketches.

4.2 Relative accuracy

Figure 13 shows the spatial and temporal development of the PM and corresponding LoD values at the sampled core points over a one-year period. The accuracy values are particularly high in the central part of the RoI – in proximity to the central camera – and as expected decrease concentrically with increasing distance. Lateral accuracy at close range is approximately 2 mm, gradually deteriorating to up to 30 mm at the outer edges of the RoI. The standard deviation of the time series is less than 1 mm in the near range and increases up to 3 mm at larger distances. Correspondingly, height accuracy is about 2 - 3 mm at close range and increases to around 11 mm at greater distances. The standard deviation of the height accuracy of the time series is more uniform with values of about 1 mm.

As the LoD values are derived from the PMs, they exhibit the same concentric spatial pattern. At close range, LoD values typically range between 5-8 mm, increasing beyond 10 mm at distances of about 6 m. The standard deviation of the LoD time series throughout the RoI amounts between 1-2 mm. Regarding temporal stability, the lateral accuracy can be considered stationary over the one-year observation period, with average values consistently below 2.5 mm. However, height accuracy and LoD values increase from < 2 mm to 3 mm and from < 5 mm to 7 mm, respectively. The farther the points are from the

https://doi.org/10.5194/egusphere-2025-2291
Preprint. Discussion started: 28 May 2025

camera setup, the more fluctuated their errors are. It is also observable that during two periods the errors are significantly larger. The first period is in December of 2020, the second one is in April of 2021.

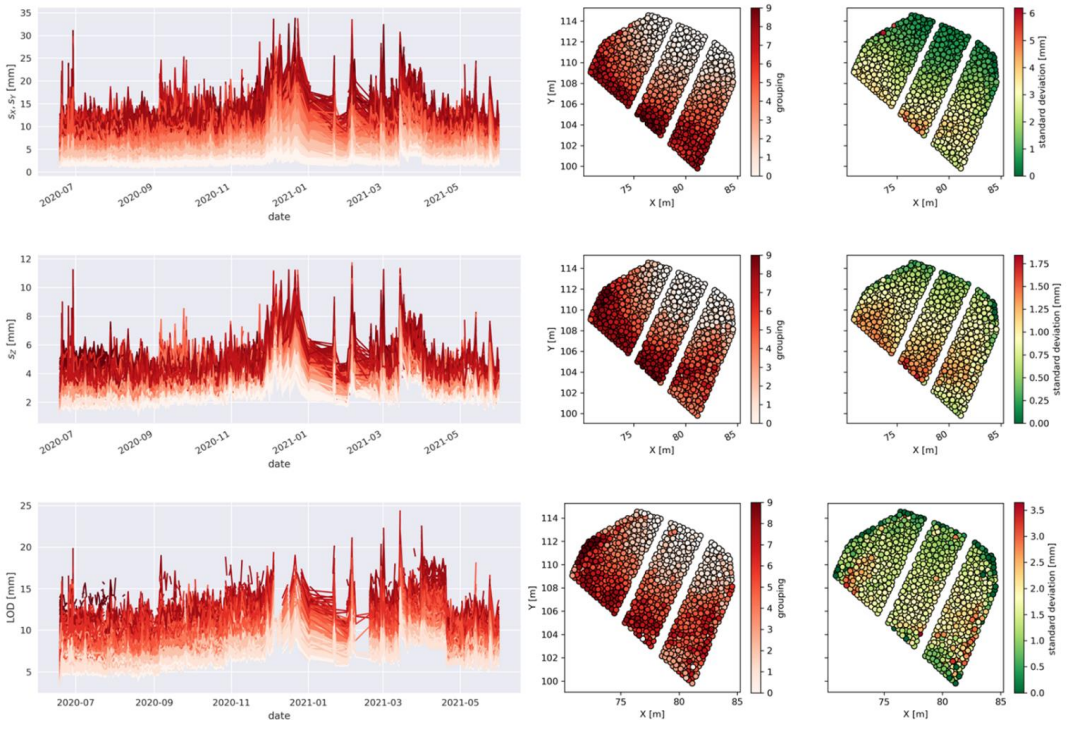

Figure 13: Variation of lateral deviation sX, sY (top row), height deviation sZ (mid row) and LoD from M3C2-PM calculation (bottom row) on evenly distributed core points. Left-hand group of diagrams shows the development of the respective parameter over a period of one year. The middle group of diagrams shows the spatial distribution of each point, colored by its respective accuracy group label. The right-hand group shows the core points underlying timeseries' standard deviation around the mean of the time series.

4.3 Level of detection for different events

Figure 14 shows the M3C2 distances (top row) and corresponding significant changes (middle row) for three selected epochs, each representing a different stage of soil surface changes: no visible erosion, light changes, and strong changes.

The first epoch (2021-07-25), captured one day after the reference (and four days after tillage), was recorded under dry conditions with no rainfall. The M3C2-calculated height differences range from slightly negative to approximately +3 mm. suggesting minimal surface changes (Fig 14a). There are some minor movements of aggregates potentially due to gravitational processes shortly after the field had been processed, indicated by large positive and negative distances in local spots. Most significant changes are concentrated on the field flanks, with the right edge showing the most pronounced activity, whereas the other areas are less noticeable (Fig 14d).

The second epoch (2021-07-31), following some minor rainfall of 8.7 mm, reveals more areas of local significant change larger than 6 mm in the central RoI (Fig 14e). Additionally, an overall lowering of the whole soil surface by 3-5 mm is observed (Fig 14b). However, this change is below the minimum detectable threshold (LoD = 6 mm) and is therefore not classified as significant.

The third epoch (2021-08-04), following heavy rainfall (27.8 mm) recorded on the previous day, shows pronounced erosion patterns. In contrast to the second epoch, height changes range between 10-60 mm (Fig 14c). Notably, rill erosion patterns become clearly visible, indicating substantial surface runoff and sediment transport in response to the intense precipitation. (no Fig 14f)

https://doi.org/10.5194/egusphere-2025-2291
Preprint. Discussion started: 28 May 2025

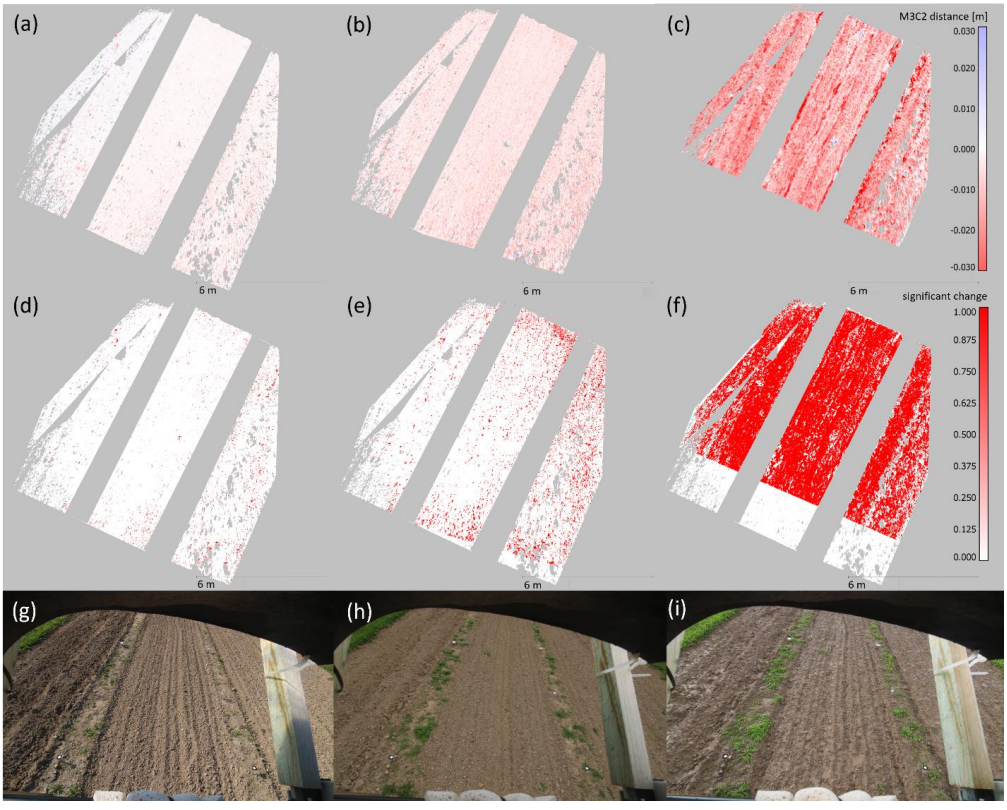

Figure 14: M3C2 (multiscale model to model cloud comparison) distance (top row), the significant changes (middle row), and images of the area of interest (bottom row) on the days of the 2021-07-25 at the middle slope one day after reference (a,d,g – left column), 2021-07-31 after an accumulated rainfall of 8.7 mm within four days (b,e,h – center column) and on the 2021-08-04 after a heavy rainfall event with 27.8 mm (c,f,i – right column).

4.4 Observing soil surface changes

Initial interpretations of the generated time series can be drawn from Fig. 15, which compares M3C2-derived elevation changes across the lower, middle, and upper slope segments, alongside rainfall, temperature, and snow cover over a three-year and four-month observation period. The lower slope – characterized by a gradient of up to 14% and not yet functioning as an accumulation zone – exhibits the most pronounced elevation changes. This can be attributed to its steep inclination and the substantial upslope contributing area, which facilitates high volumes and velocities of overland flow. Sudden and substantial decreases in elevation consistently follow periods of intense or prolonged rainfall. Notably, strong elevation responses can also be triggered by smaller rainfall events occurring within a few days after tillage (see Fig. 18 and 19). During intense rainfall events, erosion occurs primarily in the form of interrill erosion, though rill erosion is occasionally observed at the lower slope. Major rainfall episodes in July and August 2021, for instance, led to rapid surface lowering, with average elevation losses reaching up to 1 cm. The most significant changes tend to occur immediately after tillage, when the soil surface is loose and bulk density is low, resulting in both erosional and non-erosional processes such as compaction and consolidation (Kaiser et al., 2018, Epple et al., 2025). Even relatively minor rainfall events – such as those in October 2021 – can induce substantial elevation changes when occurring shortly after field cultivation.

https://doi.org/10.5194/egusphere-2025-2291
Preprint. Discussion started: 28 May 2025

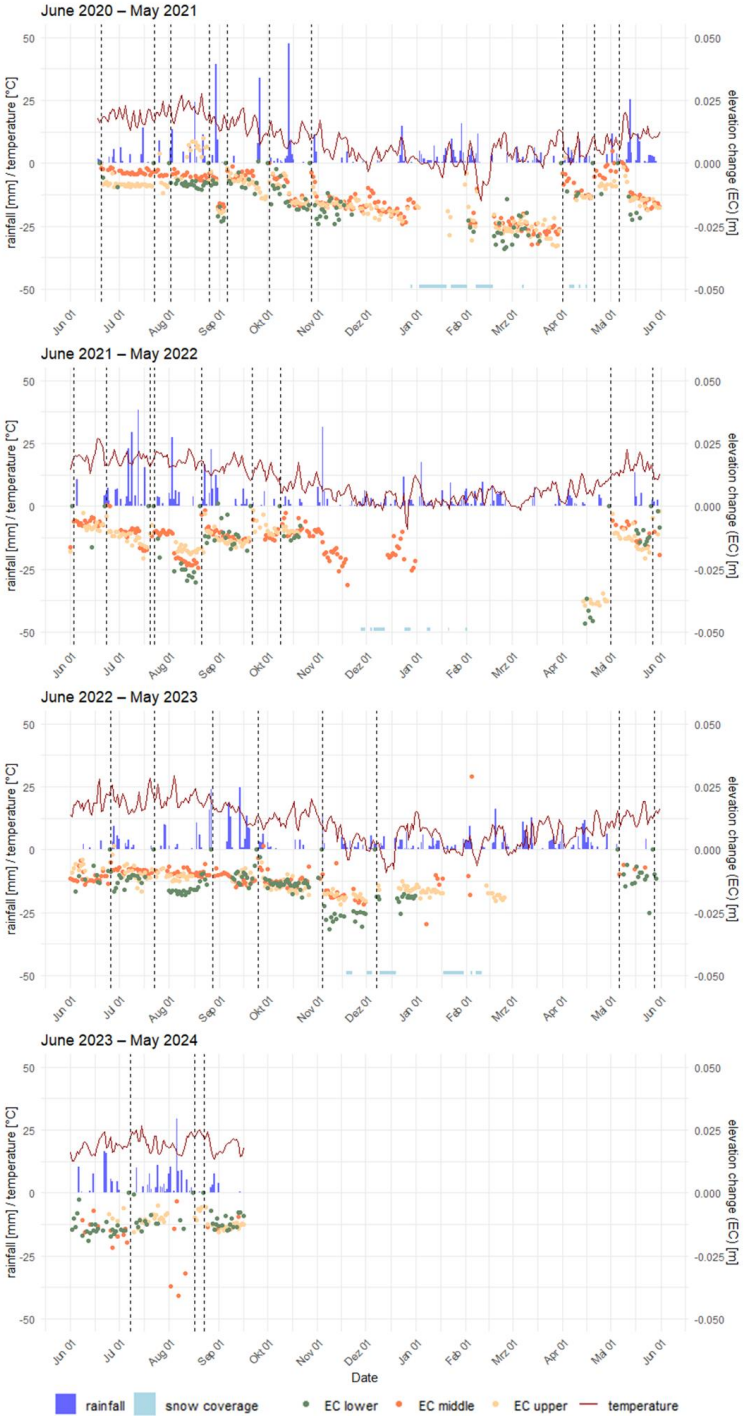

Figure 15: Temporal comparison of the daily M3C2 height changes for the lower, middle, and upper slope position (EC lower, EC middle, EC upper, where EC = elevation change), snow coverage of the slope (covered/ not covered) and the precipitation and temperature data of the weather station (landwirtschaft.sachsen.de,station Nossen – NOS) for the period June 2020 until September 2023. Vertical dotted lines = soil tillage/ new reference day.

https://doi.org/10.5194/egusphere-2025-2291
Preprint. Discussion started: 28 May 2025

Beyond providing insights into individual rainfall events, the time series also enable the assessment of seasonal developments, particularly during the winter months. On days with snow cover – indicated in Fig. 15 by light blue markers along the bottom – elevation change measurements are not possible, as the soil surface is obscured and image matching fails due to the lack of surface texture. Exceptions are observed on 2023-02-24 and 2021-04-08 (Fig. 16b and a), where positive elevation changes of +2.9 cm and +0.5 cm, respectively, were detected as a result of intense frost. Between November and April, a general elevation decrease ranging from 3-5 cm is evident, attributed to both late autumn rainfall events (e.g., November 2021) and snowmelt processes, as reflected in the February 2021 data.

Occasional positive elevation changes during this period can also result from factors unrelated to frost. For example, substantial vegetation growth before and after 2020-08-22, led to an elevation increase of up to +1.0 cm (Fig. 16c). On this particular day, the combined presence of vegetation and water accumulation from a recent precipitation event contributed to an average elevation rise of +1 cm. Similarly, in August 2023, dense vegetation growth on the upper slope (Fig. 16d) had a measurable impact on the overall elevation change. Figure 16e further illustrates how even sparse vegetation can contribute to local elevation increases, underscoring the importance of accounting for vegetation dynamics in the interpretation of erosion processes. A vegetation detection approach, based on machine learning, introduced by Grothum et al. (2023) presents a promising solution and could be applied to this dataset for improved vegetation filtering.

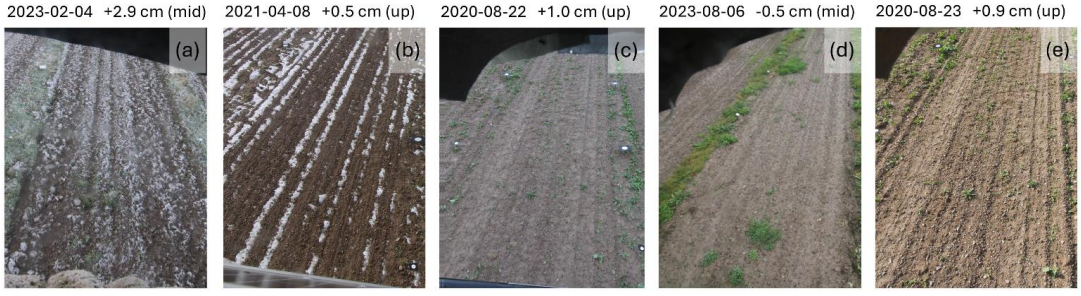

Figure 16: Images on days of positive elevation changes/ positive development. (a) and (b) show examples of positive changes due to intense frost, in (c) during a rainfall event water covered areas arise on the surface, (d) is a combination of water coverage and plant growth of a few large plants and (e) pictures small plants all over the area of interest. The date, the elevation change in respect to the reference data, and the slope position are noted above.

Data gaps occurred for several reasons. In November 2021, severe storm damage to the monitoring posts on both the lower and upper slopes resulted in extended data gaps for these positions (Tab. 1). Attempts to reconstruct the monitoring system were repeatedly hindered by adverse weather conditions and consequently an impassable surface for heavy machinery, delaying full functionality of camera systems until April 2022. Another system failure was recorded between 2023-02-25 and 2023-05-03. Table 1 summarizes the total number of survey days, excluding these long-term gaps. Additional daily data gaps arise when more than two cameras per post fail to capture usable compatible images, as 3D models require a minimum of three images for robust calculation.

Table 1: Statistics of the entire survey period 2020-06-18 until 2023-09-15

Slope position	**lower**	**middle**	**upper**
Survey period in days*	1174	1314	1155
Days on which 3D models could be created [%]**	61	67	80
Of this, days with defective 3D models* [%]**	9	9	14
Total of usable days [%]	55	61	69

**without long-term data gaps due to e.g., storm damage*
***e.g., at least three images for 3D model generation*
****GCP movements due to e.g., animals, tillage, storm events*

https://doi.org/10.5194/egusphere-2025-2291
Preprint. Discussion started: 28 May 2025

Some 3D models were excluded due to defects, which may result from inaccuracies in GCPs, failed GCP detection, extensive vegetation growth, snow cover, water cover or challenging weather conditions. According to these limitations, data is available for 55-69% of the total survey days, providing insights into both daily and seasonal elevation change trends. The lower measurement station showed an exceptional amount of outliers, due to irregular outage of camera systems.

Analysis of the variogram categorized by rainfall amount reveals that during the first 17 days following soil cultivation, variance remains consistently low across all precipitation classes (Fig. 17). After this period, accumulated low, medium, and high rainfall levels are associated with a noticeable increase in semivariance, with the most pronounced effects observed for medium and high precipitation intensities. As the time since tillage increases, precipitation can accumulate over several preceding days while also intense rainfall events may occur. Both scenarios contribute to more variable changes in surface elevation. The apparent decline in semivariance within the very high rainfall class beyond approximately 20 days is likely attributable to random noise rather than a genuine decrease in variability and should therefore be interpreted with caution. Additionally, the widening of confidence intervals with increasing time since the last tillage event further supports the trend of rising variability. Overall, Fig. 17 suggests a key threshold occurs around day 16 post-tillage, marking a notable shift in elevation change dynamics.

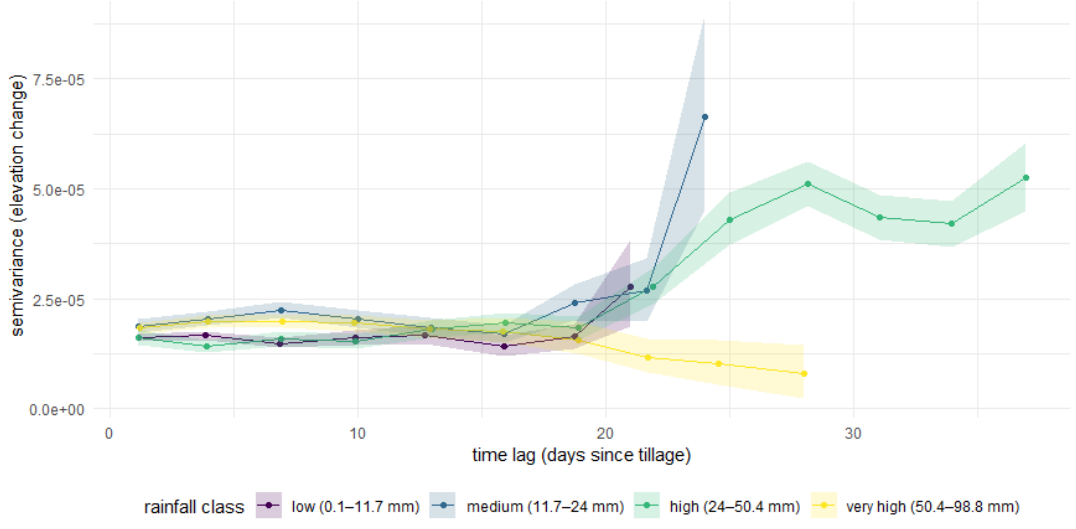

Figure 17: Directed temporal variogram of elevation change and days since last tillage with a 95% confidence interval (lag width = 3). The data is grouped by rainfall intensity into four classes divided by 25%-quantiles.

As shown in Fig. 18, all slope positions exhibit a negative trend: the higher the accumulated rainfall amount, the greater the accumulated elevation decrease. Contrary to expectations, no substantial differences in the strength of correlation were found between the middle and upper slope positions. While the lower slope also indicates a negative trend, this relationship is not statistically significant. This can likely be attributed to higher measurement uncertainty and more frequent data outages at the lower slope monitoring station, which compromise the reliability of the data compared to the middle and upper slope stations. Building on the variogram analysis, different time classes were established based on the duration since the last soil management event, and correlations were examined separately for the lower, middle, and upper slope positions (Fig. 19). Given the substantial increase in variance over time (Fig. 17), particular emphasis is placed on the first two time classes. These clearly show that during the initial period (days 1-7), a strong negative correlation exists between precipitation amount and surface elevation change across all slope positions ($r < -0.5$). This negative correlation decreases during days 8-15, consistent with increasing variability and accumulated rainfall events over time.

https://doi.org/10.5194/egusphere-2025-2291
Preprint. Discussion started: 28 May 2025

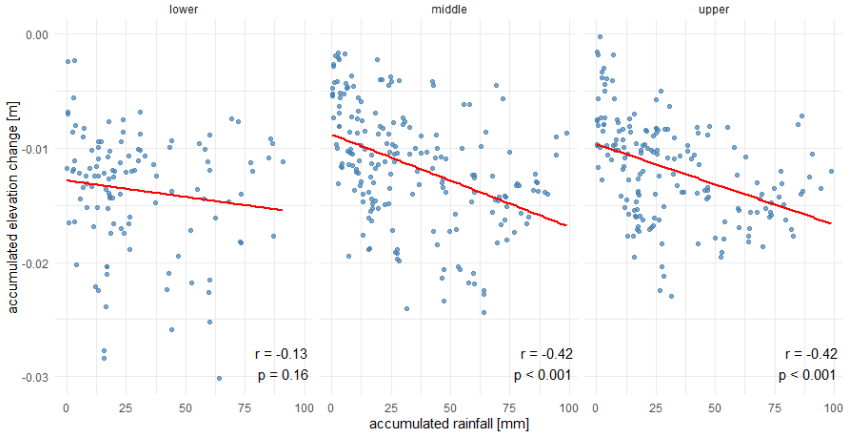

Figure 18: Scatterplot of accumulated rainfall intensity in mm and the amount of accumulated elevation change in m for the lower, middle and upper slope positions (left to right). Pearson's correlation coefficient (r) and significance (p-value) are individually noted at the bottom. The winter months as well as days with positive changes due to water or vegetation covering the surfaces are excluded from the analysis.

Fig. 20 reinforces the pattern already observed in Fig. 15: the strongest statistically significant negative correlation (r = -0.52) occurs within the first seven days following soil management, gradually diminishing across the subsequent two 'days since tillage' classes. From day 30 onward, no statistically significant correlations are observed. The initially strong negative relationship is attributed to the loose, freshly tilled soil, which is highly susceptible to compaction and settling. Even minor rainfall events during this early phase can result in substantial elevation changes, leading to a new surface level that likely reflects a 'compaction baseline'. During this period, it is difficult to clearly differentiate between non-erosional processes such as compaction and settling, and sediment yield carried downslope. Epple et al. (2025) propose an empirical approach to distinguish between these processes using high-resolution elevation change data recorded at 20-second intervals. However, their approach has not yet been tested on the broader temporal scales represented in this dataset. After this initial phase, surface elevation changes are more likely attributable to erosional processes. Small rainfall events tend to produce only minor changes, while larger events are required to generate more pronounced elevation decrease.

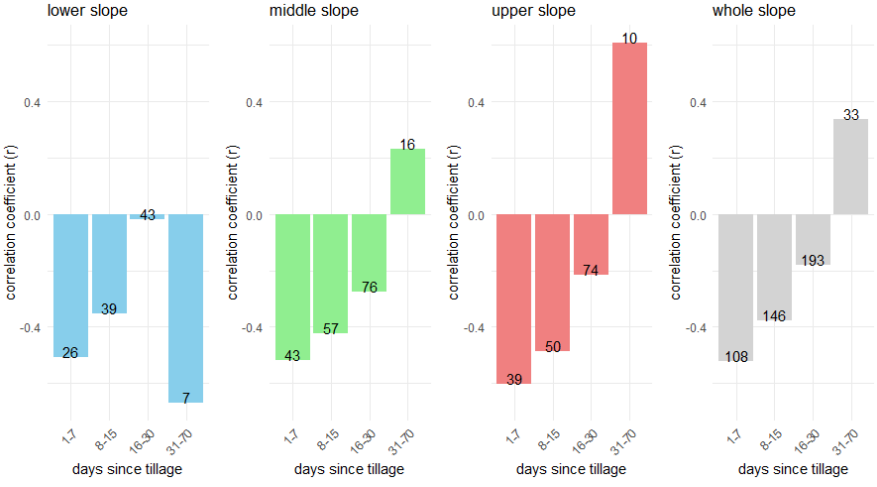

Figure 19: Pearson's correlation (r) of rainfall intensity with elevation changes of the day after the rainfall event. Calculated for the whole slope and for all three slope positions individually. These correlations are calculated within predefined time bins of days passed since the last tillage. The count of valid observations for each bin is displayed along the bars. The winter months as well as days with changes due to water or vegetation covering the surfaces are excluded from the analysis.

https://doi.org/10.5194/egusphere-2025-2291
Preprint. Discussion started: 28 May 2025

The color gradient in Fig. 20 further indicates that, during the later period (days 16-30), greater elevation changes are associated with areas that had already experienced higher accumulated rainfall in the preceding days. Compared to the first time class – dominated by a mix of erosional and non-erosional processes – these later stages require greater cumulative rainfall to produce elevation changes exceeding -0.02 m.

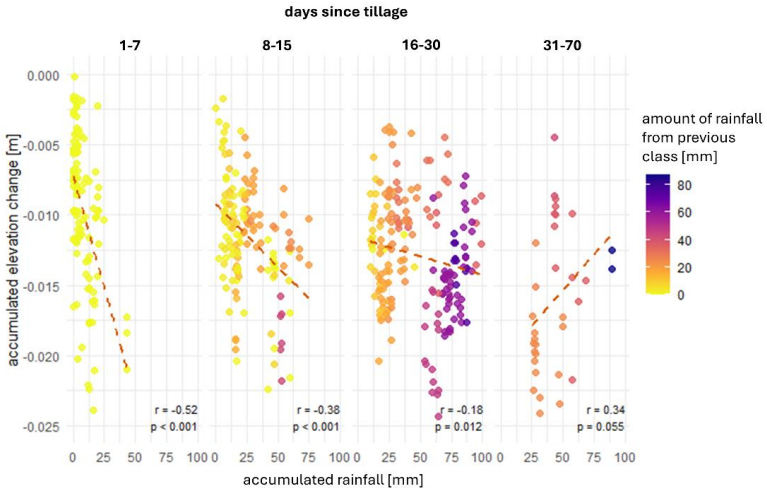

Figure 20: Scatter plots correlating accumulated rainfall intensity in mm and accumulated elevation change in m for the whole slope, divided into four bins – days since last tillage on the slope. The data points are colored considering the amount of rainfall fallen in the previous bin. Pearson's correlation coefficient (r) and the significance (p-value) for each bin are noted at the bottom.

4.5 System Evaluation and Recommendations

The time-based trigger system consistently provided daily observations of the soil surface over an extended period. The comparison of the camera rig-based 3D models with the TLS and UAV data highlights the great detail of the reconstructed soil surface. Furthermore, the reconstruction accuracy and consistency are especially high in the central area, while the errors increase in the outer regions. This variance primarily stems from camera geometry; the central area benefits from coverage by all five cameras, whereas side areas are captured by only one side, resulting in inadequate ray intersection geometries. The PMs and LoDs reaffirm that the camera geometry significantly impacts point precision. The stationary behavior of lateral accuracy contrasts with the slight increase in height errors and LoD over time, suggesting potential changes in camera calibration, particularly in distortion parameters. Two notable data gaps with elevated values are attributed to adverse weather and surface conditions, such as prolonged snow cover (January, February and December 2021).

This study presents a novel observation system to study natural rain-driven soil surface change processes. To enhance its functionality, several improvements are suggested. The implementation of a telemetric system is proposed to relay operational status information, including malfunctions, errors, and battery levels of both the master station and cameras, to a centralized hub. This centralized hub can serve as a focal point for data management, allowing for the establishment of an integrated pipeline from data acquisition through to processing. By recognizing failing cameras at an early stage, problems can be rectified immediately, and a higher data density can be achieved. Furthermore, the wind direction should be carefully considered in regard of system orientation because during our observation period, especially during strong rainfall events, measurement quality decreased significantly or failed due to raindrops on the glass.

Moving forward, leveraging the generated 3D surface models for validation against soil erosion models is recommended. This comparative analysis will provide valuable insights into the applicability and efficacy of the models within the context of soil erosion modeling complexities. Such validation efforts are crucial for advancing our understanding of soil erosion processes and refining predictive modeling techniques (e.g., Eltner et al., 2025).

https://doi.org/10.5194/egusphere-2025-2291
Preprint. Discussion started: 28 May 2025

5 Conclusion

We introduce a camera-based soil surface change observation to assess natural rainfall effects. Our setup comprised five cameras mounted on three sturdy wooden structures each and activated by a rain gauge through a microcontroller, facilitating event-based and time-based triggering. We established a Python-based workflow to automate image synchronization, GCP detection, point cloud processing and comparison. The resulting processed point clouds offer a detailed overview of the observed epoch in comparison to utilizing TLS or UAV photogrammetry. Notably, they exhibit minimal systematic errors, showcasing the effectiveness of our stationary observation system in capturing surface topography with greater detail.

For a comprehensive evaluation, we conducted a year-long time series analysis, comparing each epoch with a reference epoch using M3C2-PM. The standard deviation of these PMs ranges from 3 mm laterally and 2 mm vertically in the best cases to 30 mm laterally and 20 mm vertically in the worst cases. The accuracy is influenced by the distance from the cameras and the position of points relative to the camera station, with the LoD varying between 5 mm at best and 25 mm at worst.

Our established workflow is readily transferable to similar experimental settings. The resulting unique dataset provides valuable insights into both daily and seasonal dynamics of soil elevation changes. Notably, the most significant changes occur even after relatively low rainfall events following agricultural tillage, likely due to a combination of erosional and non-erosional processes. A consistent decline in elevation is observed throughout the winter months. This data generation approach enables the analysis of erosion development at high spatial and temporal resolutions during individual rainfall events, while also capturing broader seasonal trends. Future research should focus on the modeling and validation of soil erosion models to evaluate the relevance and potential of the generated soil surface data in advancing soil erosion prediction and management.

Data and Code availability

The hardware to capture the image data, including the source code for its control, are provided in the appendix. The Python scripts for the time lapse data processing are provided here: https://github.com/onlyole/TimeLapseErosion.git. The image data and processed point clouds (of change) will be provided in a separate data publication.

ACKNOWLEDGEMENTS

The study was supported by the German Research Foundation (DFG) under the project number 405774238: *High resolution photogrammetric methods for nested parameterization and validation of a physical based soil erosion model*. We also extend our sincere thanks to the team of the 'Versuchsstation Nossen' of the LfULG Saxony for their invaluable technical support and assistance throughout the monitoring campaign. During the revision of the manuscript, we used ChatGPT (GPT-4o) to improve the readability and language of the text. After using the tool, we carefully reviewed and edited the content as needed to ensure correctness and originality. We take full responsibility for the final content. The supplement with the animations can be found here: 10.5281/zenodo.15526699.

References

Agisoft LLC, 2022: Metashape Professional Edition – User Manual, Version 1.8. Available at: https://www.agisoft.com/pdf/metashape-pro_1_8_en.pdf (last access: 7 May 2025).

Anders, K., Winiwarter, L., Mara, H., Lindenbergh, R., Vos, S. E., and Höfle, B.: Fully Automatic Spatiotemporal Segmentation of 3D LiDAR Time Series for the Extraction of Natural Surface Changes, ISPRS J. of Photogram. and Remote Sens, 173, 297–308, https://doi.org/10.1016/j.isprsjprs.2021.01.015, 2021.

https://doi.org/10.5194/egusphere-2025-2291
Preprint. Discussion started: 28 May 2025

Balaguer-Puig, M., Marqués-Mateu, Á., Lerma, J. L., and Ibáñez-Asensio, S.: Estimation of small-scale soil erosion in laboratory experiments with Structure from Motion photogrammetry, Geomorphology, 295, 285–296, https://doi.org/10.1016/j.geomorph.2017.04.035, 2017.

Batista, P. V. G., Davies, J., Silva, M. L. N., and Quinton, J. N.: On the Evaluation of Soil Erosion Models: Are We Doing Enough?, Earth-Science Reviews, 197, https://doi.org/10.1016/j.earscirev.2019.102898, 2019.

Bay, H., Tuytelaars, T., and Gool, L.: SURF: Speeded Up Robust Features, in: Computer Vision – ECCV 2006, vol. 3951, edited by: Leonardis, A., Bischof, H., and Pinz, A., Springer, Berlin, Heidelberg, 404–17, https://doi.org/10.1007/11744023_32, 2006.

Besl, P. J. and McKay, N. D.: A Method for Registration of 3-D Shapes, IEEE Transactions on Pattern Analysis and Machine Intelligence, 14, 239–56, https://doi.org/10.1109/34.121791, 1992.

Blanch, X., Jäschke, A., Elias, M., Eltner, A.: Sub-pixel automatic detection of GCPs coordinates in time-lapse images using a Deep Learning keypoint network. IEEE Transactions on Geosciences and Remote Sensing, https://doi.org/10.1109/TGRS.2024.3514854, 2025.

Blanch, X., Eltner, A., Guinau, M., and Abellan, A.: Multi-Epoch and Multi-Imagery (MEMI) Photogrammetric Workflow for Enhanced Change Detection Using Time-Lapse Cameras, Remote Sensing, 13, https://doi.org/10.3390/rs13081460, 2021.

Blanch, X., Guinau, M., Eltner, A., and Abellan, A.: Fixed photogrammetric systems for natural hazard monitoring with high spatio-temporal resolution, Natural Hazards and Earth System Sciences, 23, 3285–3303, https://doi.org/10.5194/nhess-23-3285-2023, 2023.

Blanch, X., Guinau, M., Eltner, A., and Abellan, A.: A cost-effective image-based system for 3D geomorphic monitoring: an application to rockfalls, Geomorphology, 449, 109065, https://doi.org/10.1016/j.geomorph.2024.109065, 2024.

Blistan, P., Jacko, S., Kovanič, Ľ., Kondela, J., Pukanská, K., and Bartoš, K.: TLS and SfM Approach for Bulk Density Determination of Excavated Heterogeneous Raw Materials, Minerals, 10, https://doi.org/10.3390/min10020174, 2020.

Borrelli, P., Robinson, D. A., Fleischer, L. R., Lugato, E., Ballabio, C., Alewell, C., Meusburger, K., Modugno, S., Schütt, B., Ferro, V., Bagarello, V., Oost, K. V., Montanarella, L., and Panagos, P.: An assessment of the global impact of 21st century land use change on soil erosion, Nature Communications, 8, https://doi.org/10.1038/s41467-017-02142-7, 2017.

Brown, D.: Close-Range Camera Calibration, Photogrammetric Engineering & Remote Sensing, 37, 855–66, 1971.

Cândido, B. M., Quinton, J. N., James, M. R., Silva, M. L. N., Carvalho, T. S., Lima, W., Beniaich, A., and Eltner, A.: High-Resolution Monitoring of Diffuse (Sheet or Interrill) Erosion Using Structure-from-Motion, Geoderma, 375, https://doi.org/10.1016/j.geoderma.2020.114477, 2020.

Chen, Y. and Medioni, G.: Object Modeling by Registration of Multiple Range Images, in: Proceedings. 1991 IEEE International Conference on Robotics and Automation, Sacramento, CA, USA, 2724–29, 1991.

Cloudcompare (version 2.13.2) [GPL software]. Retrieved from http://www.cloudcompare.org, 2024.

Dai, W., Qian, W., Liu, A., Wang, C., Yang, X., Hu, G., and Tang, G.: Monitoring and modeling sediment transport in space in small loess catchments using UAV-SfM photogrammetry, Catena, 214, https://doi.org/10.1016/j.catena.2022.106244, 2022.

Doetterl, S., Berhe, A. A., Nadeu, E., Wang, Z., Sommer, M., & Fiener, P.: Erosion, deposition and soil carbon: A review of process-level controls, experimental tools and models to address C cycling in dynamic landscapes. Earth-Science Reviews, 154, 102–122. https://doi.org/10.1016/j.earscirev.2015.12.005, 2016.

Eldar, Y., Lindenbaum, M., Porat, M., and Zeevi, Y. Y.: The Farthest Point Strategy for Progressive Image Sampling, IEEE Transactions on Image Processing, 6, 1305–15, https://doi.org/10.1109/83.623193., 1997.

Eltner, A. and Schneider, D.: Analysis of Different Methods for 3D Reconstruction of Natural Surfaces from Parallel-Axes UAV Images, The Photogrammetric Record, 30, 279–99, https://doi.org/10.1111/phor.12115, 2015.

Eltner, A., Baumgart, P., Maas, H. G., and Faust, D.: Multi-temporal UAV data for automatic measurement of rill and interrill erosion on loess soil, Earth Surface Processes and Landforms, 40, 741–755, https://doi.org/10.1002/esp.3673, 2015.

https://doi.org/10.5194/egusphere-2025-2291
Preprint. Discussion started: 28 May 2025

Eltner, A., Kaiser, A., Castillo, C., Rock, G., Neugirg, F., and Abellán, A.: Image-Based Surface Reconstruction in Geomorphometry – Merits, Limits and Developments, Earth Surface Dynamics, 4, 359–89, https://doi.org/10.5194/esurf-4-359-2016, 2016.

Eltner, A., Kaiser, A., Abellan, A., and Schindewolf, M.: Time Lapse Structure-from-motion Photogrammetry for Continuous Geomorphic Monitoring, Earth Surface Processes and Landforms, 42, 2240–53, https://doi.org/10.1002/esp.4178, 2017.

Eltner, A., Maas, H.-G., and Faust, D.: Soil Micro-Topography Change Detection at Hillslopes in Fragile Mediterranean Landscapes, Geoderma, 313, 217–32, https://doi.org/10.1016/j.geoderma.2017.10.034, 2018.

Eltner, A., Favis-Mortlock, D., Grothum, O., Neumann, M., Laburda, T., and Kavka, P.: Using 3D observations with high spatio-temporal resolution to calibrate and evaluate a process-focused cellular automaton model of soil erosion by water, https://doi.org/10.5194/egusphere-2024-2648, 2025.

Epple, L., Kaiser, A., Schindewolf, M., Bienert, A., Lenz, J., and Eltner, A.: A Review on the Possibilities and Challenges of Today's Soil and Soil Surface Assessment Techniques in the Context of Process-Based Soil Erosion Models, Remote Sensing, 14, https://doi.org/10.3390/rs14102468, 2022.

Epple, L., Grothum, O., Bienert, A., Eltner, A.: Decoding rainfall effects on soil surface changes: Empirical separation of sediment yield in time-lapse SfM photogrammetry measurements. Soil & Tillage Research, 248, 106384. 10.1016/j.still.2024.106384, 2025

Evans, D. L., Cândido, B., Coelho, R. M., Maria, I. C. D., Moraes, J. F. L. de, Eltner, A., Martins, L. L., and Cantarella, H.: The Loss of Soil Parent Material: Detecting and Measuring the Erosion of Saprolite, Soil Systems, 8, https://doi.org/10.3390/soilsystems8020043, 2024.

Fabbri, R., Giblin, P., and Kimia, B.: Camera Pose Estimation Using First-Order Curve Differential Geometry, IEEE Transactions on Pattern Analysis and Machine Intelligence, 43, 3321–32, https://doi.org/10.1109/TPAMI.2020.2985310, 2021.

Fiener, P., Dostál, T., Krása, J., Schmaltz, E., Strauss, P., and Wilken, F.: Operational USLE-Based Modelling of Soil Erosion in Czech Republic, Austria, and Bavaria-Differences in Model Adaptation, Parametrization, and Data Availability, https://doi.org/10.3929/ethz-b-000418650, 2020.

Godding, R. and Luhmann, T.: Calibration and Accuracy Assessment of a Multi- Sensor Online- Photogrammetric System, in: International Archives of Photogrammetry and Remote Sensing XXIX:24–29, 1992.

Grothum, O., Bienert, A., Bluemlein, M., and Eltner, A.: USING MACHINE LEARNING TECHNIQUES TO FILTER VEGETATION IN COLORIZED SFM POINT CLOUDS OF SOIL SURFACES, Int. Arch. Photogramm. Remote Sens. Spatial Inf. Sci., XLVIII-1/W2-2023, 163–170, https://doi.org/10.5194/isprs-archives-XLVIII-1-W2-2023-163-2023, 2023.

Hänsel, P., Schindewolf, M., Eltner, A., Kaiser, A., and Schmidt, J.: Feasibility of High-Resolution Soil Erosion Measurements by Means of Rainfall Simulations and SfM Photogrammetry, Hydrology, 3, https://doi.org/10.3390/hydrology3040038, 2016.

He, T., Yang, Y., Shi, Y., Liang, X., Fu, S., Xie, G., Liu, B., and Liu, Y.: Quantifying spatial distribution of interrill and rill erosion in a loess at different slopes using structure from motion (SfM) photogrammetry, International Soil and Water Conservation Research, 10, 393–406, https://doi.org/10.1016/j.iswcr.2022.01.001, 2022.

James, M. R. and Robson, S.: Straightforward Reconstruction of 3D Surfaces and Topography with a Camera: Accuracy and Geoscience Application, Journal of Geophysical Research: Earth Surface, 117, https://doi.org/10.1029/2011JF002289, 2012.

James, M. R., Robson, S., and Smith, M. W.: 3-D Uncertainty-based Topographic Change Detection with Structure-from-motion Photogrammetry: Precision Maps for Ground Control and Directly Georeferenced Surveys, Earth Surface Processes and Landforms, 42, 1769–88, https://doi.org/10.1002/esp.4125, 2017.

Jetten, V., & Favis-Mortlock, D.: Modelling Soil Erosion in Europe. In Soil Erosion in Europe (pp. 695–716). John Wiley and Sons Ltd. https://doi.org/10.1002/0470859202.ch50, 2006., 2006.

https://doi.org/10.5194/egusphere-2025-2291
Preprint. Discussion started: 28 May 2025

Karydas, C. G., Panagos, P., and Gitas, I. Z.: A classification of water erosion models according to their geospatial characteristics, International Journal of Digital Earth, 7, 229–250, https://doi.org/10.1080/17538947.2012.671380, 2014.

Kohrell, G. J., Mulla, D. J., and Gelder, B.: Calibration and validation of hillslope runoff and soil loss outputs from the Water Erosion Prediction Project model in Minnesota agricultural watersheds, Journal of the American Water Resources Association, 59, 1529–1548, https://doi.org/10.1111/1752-1688.13148, 2023.

Krimmel, R. M. and Rasmussen, L. A.: Using Sequential Photography to Estimate Ice Velocity at the Terminus of Columbia Glacier, Alaska, Annals of Glaciology, 8, 117–23, https://doi.org/10.3189/S0260305500001270, 1986.

Kromer, R., Walton, G., Gray, B., Lato, M., and Group, R.: Development and Optimization of an Automated Fixed-Location Time Lapse Photogrammetric Rock Slope Monitoring System, Remote Sensing, 11, https://doi.org/10.3390/rs11161890, 2019.

Lague, D., Brodu, N., and Leroux, J.: Accurate 3D Comparison of Complex Topography with Terrestrial Laser Scanner: Application to the Rangitikei Canyon (N-Z, ISPRS Journal of Photogrammetry and Remote Sensing, 82, 10–26, https://doi.org/10.1016/j.isprsjprs.2013.04.009, 2013.

Li, P., Ren, F., Hu, J., Yan, L., Hao, M., Liu, L., Gao, J., and Dang, T.: Monitoring soil erosion on field slopes by terrestrial laser scanning and structure-from-motion, Land Degradation and Development, 34, 3663–3680, https://doi.org/10.1002/ldr.4712, 2023.

Luhmann, T., Fraser, C., and Maas, H.-G.: Sensor Modelling and Camera Calibration for Close-Range Photogrammetry, ISPRS Journal of Photogrammetry and Remote Sensing, 115, 37–46, https://doi.org/10.1016/j.isprsjprs.2015.10.006, 2016.

Mallalieu, J., Carrivick, J. L., Quincey, D. J., Smith, M. W., and James, W. H. M.: An integrated structure-from-motion and time-lapse technique for quantifying ice-margin dynamics", J. Glaciol, 63, 937–949, 2017.

Michael, A.: Anwendung des physikalisch begründeten Erosionsprognosemodells EROSION 2D/3D - Empirische Ansätze zur Ableitung der Modellparameter, 2014.

Mohren, J., Binnie, S. A., Rink, G. M., Knödgen, K., Miranda, C., Tilly, N., and Dunai, T. J.: A Photogrammetry-Based Approach for Soil Bulk Density Measurements with an Emphasis on Applications to Cosmogenic Nuclide Analysis, Earth Surface Dynamics, 8, 995–1020, https://doi.org/10.5194/esurf-8-995-2020, 2020.

Möller, T. and Hughes, J. F.: Efficiently Building a Matrix to Rotate One Vector to Another, Journal of Graphics Tools, 4, 1–4, https://doi.org/10.1080/10867651.1999.10487509, 1999.

Panagos, P., Borrelli, P., Poesen, J., Ballabio, C., Lugato, E., Meusburger, K., Montanarella, L., and Alewell, C.: The new assessment of soil loss by water erosion in Europe, Environmental Science and Policy, 54, 438–447, https://doi.org/10.1016/j.envsci.2015.08.012, 2015.

Schindewolf, M. and Schmidt, J.: Parameterization of the EROSION 2D/3D Soil Erosion Model Using a Small-Scale Rainfall Simulator and Upstream Runoff Simulation, CATENA, 91, 47–55, https://doi.org/10.1016/j.catena.2011.01.007, 2012.

Schwalbe, E., Koschitzki, R., and Maas, H. G.: RECOGNITION OF DRAINAGE TUNNELS DURING GLACIER LAKE OUTBURST EVENTS FROM TERRESTRIAL IMAGE SEQUENCES, in: The International Archives of the Photogrammetry, Remote Sensing and Spatial Information Sciences XLI-B8:537–43, https://doi.org/10.5194/isprs-archives-XLI-B8-537-2016, 2016.

Vos, S., Anders, K., Kuschnerus, M., Lindenbergh, R., Höfle, B., Aarninkhof, S., and Vries, S.: A High-Resolution 4D Terrestrial Laser Scan Dataset of the Kijkduin Beach-Dune System, The Netherlands, Scientific Data, 9, https://doi.org/10.1038/s41597-022-01291-9, 2022.

Westoby, M. J., Brasington, J., Glasser, N. F., Hambrey, M. J., and Reynolds, J. M.: 'Structure-from-Motion' Photogrammetry: A Low-Cost, Effective Tool for Geoscience Applications, Geomorphology, 179, 300–314, https://doi.org/10.1016/j.geomorph.2012.08.021, 2012.